Separation and Purification Technology 282 (2022) 120153

Contents lists available at ScienceDirect

Separation and Purification Technology

journal homepage: www.elsevier.com/locate/seppur

Rational design of 2D ultrathin $BiO(HCOO)_xI_{1-x}$ composite nanosheets: The synergistic effect of ultrathin structure and hybridization in the effective elimination of BPA under visible light irradiation

Qiao Wang [a], Guanheng Lv [a], Yiting Cao [a], Zhenhui Chen [a], Jialin Jia [b,*], Yanlin Qin [c,1], Zhenxuan Lin [a], Xuan Xie [a], Zhihong Wang [a]

[a] School of Civil and Transportation Engineering, Guangdong University of Technology, Guangzhou 510006, China
[b] State Key Laboratory of Urban Water Resource and Environment, Harbin Institute of Technology, Harbin 150090, China
[c] School of Chemical Engineering and Light Industry, Guangdong University of Technology, Guangzhou 510006, China

ARTICLE INFO

Keywords:
2D ultrathin nanosheet
Hybrid composite
Bismuth oxide formate
Visible-light photocatalysis
BPA degradation

ABSTRACT

Here, a novel series of 2D $BiO(HCOO)_xI_{1-x}$ composites were first fabricated with a ultrathin thickness (~2.47 nm). Among them, the optimal $BiO(HCOO)_{0.75}I_{0.25}$ nanosheets exhibited a superior photocatalytic performance with the kinetic constant reaching up to 0.2148 min^{-1}, which was 5.9, 97.6 and 27.2 folds higher than that of pristine BiOI, BiOCOOH and $BiO(HCOO)_{0.75}I_{0.25}$-P nanoplates, respectively. Benefiting from the synergistic effect of ultrathin two-dimensional structure and hybrid composite, the photocatalytic performance was signally improved. Based on the optical and photoelectrochemical characterizations, the fabrication of hybrid composite delivered the optimal balance of visible-light absorption and redox capacity, endowing the photoinduced holes a higher oxidation potential. Meanwhile, the construction of 2D ultrathin structure reduced the migration distance of charge carriers, consequently accelerated those separated rate. This study provides a new insight for designing high active Bi-based photocatalysts, which is hopeful to make a great contribution to aquatic environmental restoration.

1. Introduction

The presence of endocrine disrupter chemicals (EDCs) has been regarded as an emerging problem in water and wastewater treatment, as well as sediment recovery [1]. Various laboratory studies manifested that EDCs would exhibit a endocrine disrupting effect and the toxicity to cells, genes and nerves of the aquatic organisms and human beings, which desperately needed to be controlled [2,3]. For addressing this urgent issue, semiconductor photocatalytic technology has received continued attention since it was always deemed as a green, economic and efficient method to eliminate refractory contaminants [4–6].

Among various semiconductors photocatalysts, Bi-based materials, such as Bi_2MoO_6 [7,8], $BiVO_4$ [9,10], Bi_2WO_6 [11], BiOX [12]and BiOCOOH [13] have been intensively studied due to their excellent photocatalytic activity. As a member of the Sillén family, bismuth oxide formate (BiOCOOH) owns layered structure with $[Bi_2O_2]^{2+}$ slab and serrated $COOH^-$ [14], which can modulate the electronic structure and accordingly accelerate the separation of photogenerated charge carries [15]. Moreover, it owns more "green" elements of O, C and H, which can avoid secondary pollution to the environment.

Nevertheless, due to the large band gap (~ 3.30 eV), BiOCOOH only responds to ultraviolet light [16]. Meanwhile, the single-component of BiOCOOH still faces the shortage of the fast photoinduced electrons-holes pairs and low photo quantum efficiency [17], just like most intrinsic semiconductor materials. Recently, constructing hybrid composite structures have gain great interest since it can constantly regulate band structures, leading to the optimal equilibrium of light absorption and redox ability, and consequently benefit the photocatalytic performance [18,19]. Due to its merits, hybrid composite strategy has been widely adopted in establishing various excellent photocatalysts, such as $Bi_2W_{1-x}Mo_xO_6$ [20], $Zn_3In_2S_6$ [21] and $(GaN)_{(1-x)}(ZnO)_x$ [22], etc. As a narrow bandgap semiconductor (Eg = ~1.8 eV), bismuth oxyiodide (BiOI) possesses outstanding light absorption ability and high carriers separation rate. Many studies have reported that the combination of

* Corresponding author.
E-mail addresses: huaiqiu1234@126.com (J. Jia), ylqin@gdut.edu.cn (Y. Qin).
[1] Co-corresponding author.

https://doi.org/10.1016/j.seppur.2021.120153
Received 16 September 2021; Received in revised form 14 November 2021; Accepted 14 November 2021
Available online 16 November 2021

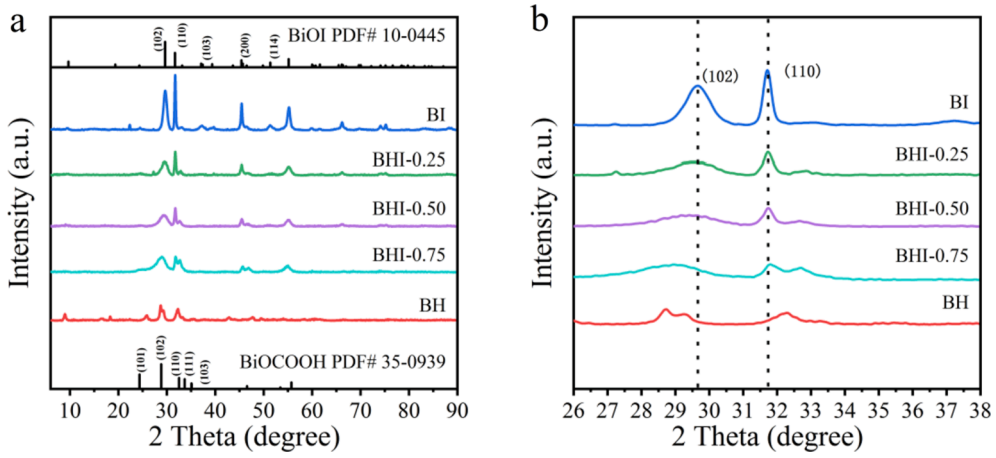

Fig. 1. (a) XRD patterns of BHI-x composites (x = 1, 0.75, 0.50, 0.25, 0) and (b) the corresponding amplifying spectra.

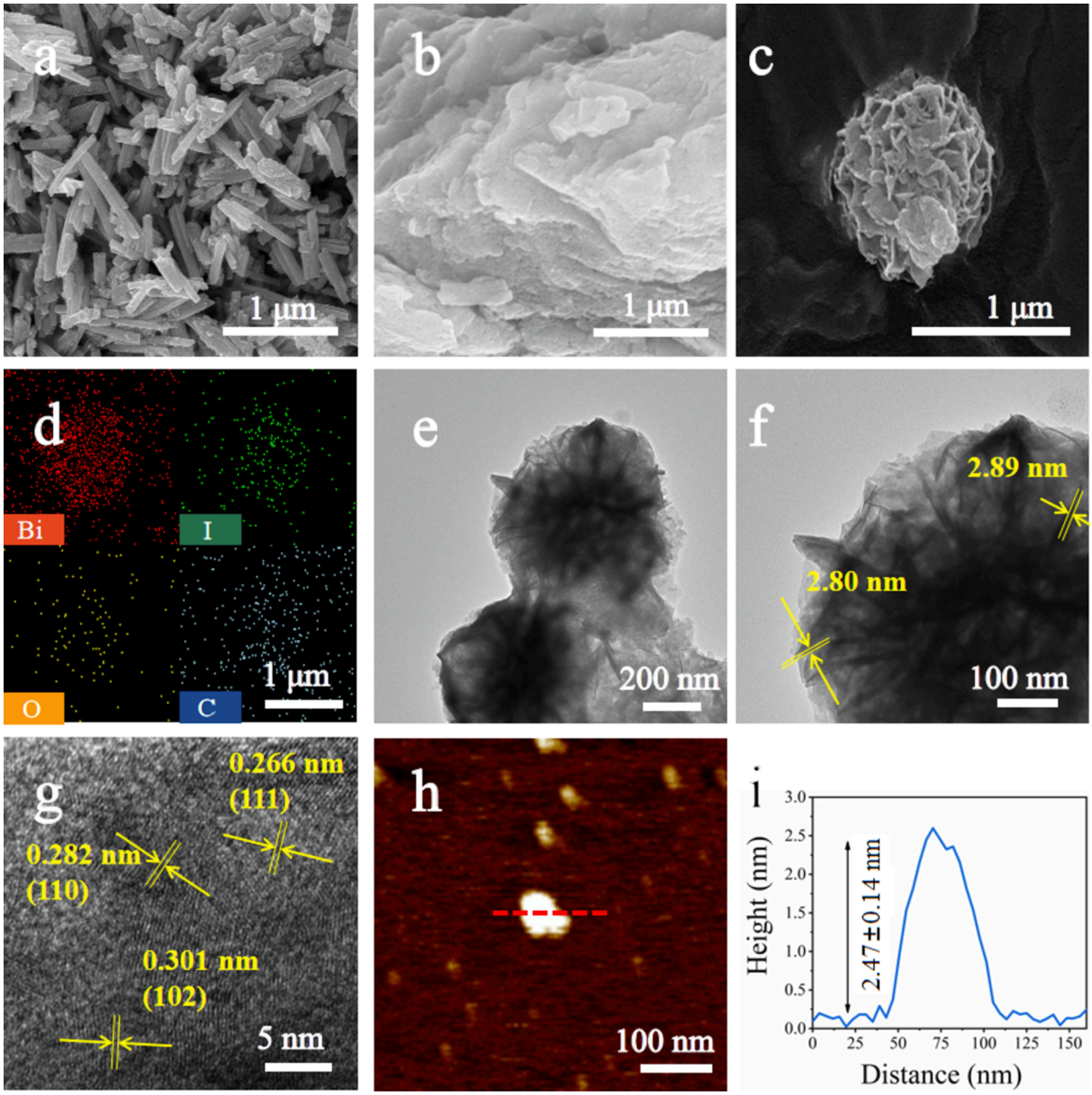

Fig. 2. SEM images of (a) BH nanorods, (b) BI nanosheets, (c) ultrathin BHI-0.75 nanosheets; (d) SEM-EDS mapping images of BHI-0.75, (e-f) TEM images and (g) HRTEM image of BHI-0.75, (h-i) AFM image and corresponding height curve of BHI-0.75.

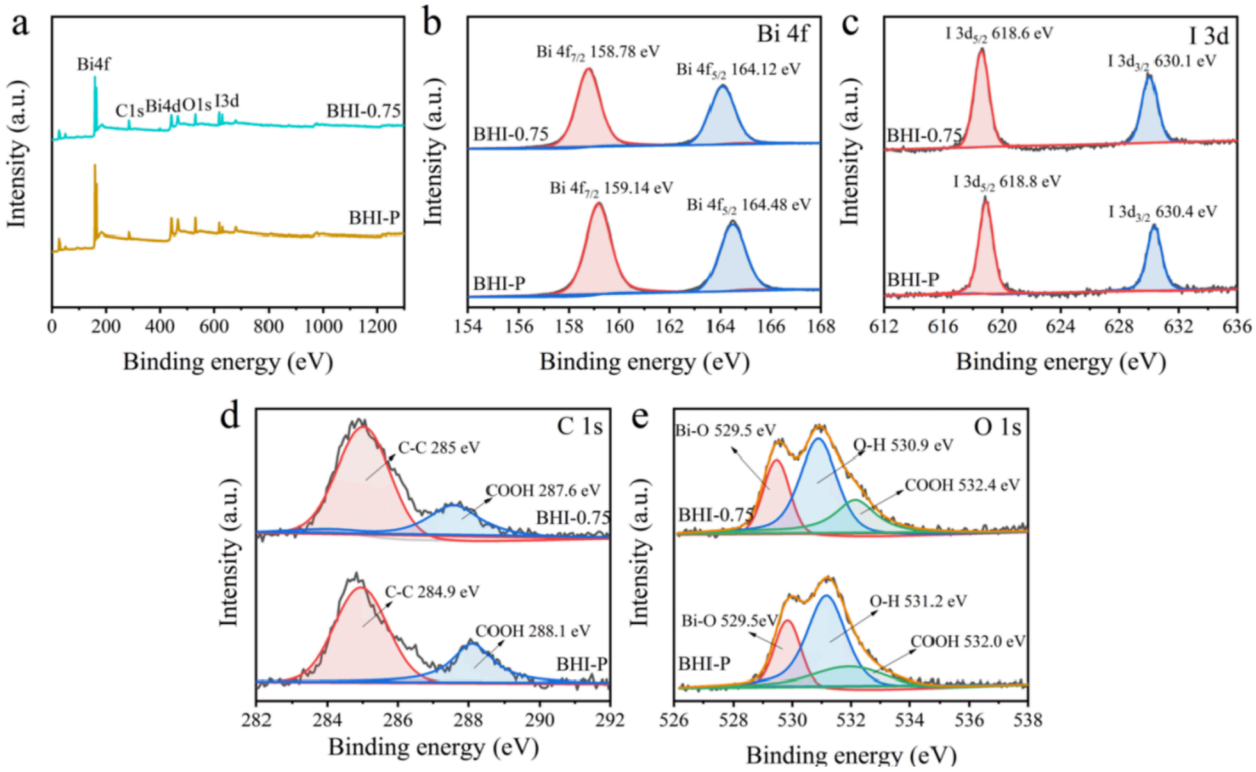

Fig. 3. XPS spectra of ultrathin BHI-0.75 nanosheets and BHI-P nanoplates: (a) survey, (b) Bi 4f, (c) I 3d, (d) C 4f and (e) O 1 s spectrum.

semiconductor and BiOI can remarkably improve the photocatalytic performance, for example, $BiOBr_xI_{1-x}$ [23], BiOI/MIL-125(Ti) [24] and BiO_xCl_y/BiO_mI_n composites [25]. The boosted photocatalytic activity in previous studies motivates us to attempt this strategy in modifying BiOCOOH and further applying to restoring water environment. However, limited research concerns BiOCOOH-BiOI hybrid composite preparation, photocatalytic activity and oxidation mechanism, which desiderates to be strengthened and perfected.

Meanwhile, in the past decade, designing ultrathin 2D materials have been considered as a brilliant star in various applications such as energy storage and conversion, optoelectronic devices, field effect transistors, and catalysis [26–30]. Ultrathin 2D materials, typically with the thickness of less than 5 nm, always possess large surface area and short charge transfer distance, which largely favour the photocatalytic reaction. Generally, the light absorption of the nanosized particles or bulk materials are limited by reflection at the grain boundaries and light transmittance [31], whereas 2D materials offer a planar region for adsorbing light to the greatest extent. Compared to bulk materials, the charge carriers migration distance of 2D materials is greatly reduced due to the atomic thickness, which make the photoinduced charges quickly transferred to the surface of the catalysts, thus remarkably inhibit the recombination of photoinduced charge carriers [32]. Inspired by above consideration, a satisfactory photocatalytic performance should be predictable if the 2D ultrathin composite of BiOCOOH and BiOI are fabricated.

Hence, in this work, the ultrathin $BiO(HCOO)_xI_{1-x}$ hybrid composite nanosheets (~2.47 nm thickness) were rational designed as a model catalyst via a facile solvothermal method, and employed to degrade BPA for evaluating the photocatalytic activity. Benefitting the synergistic effect of ultrathin structure and hybrid composite, the as-prepared sample is expected to achieve notably enhanced photocatalytic performance in BPA elimination. In addition, the photocatalytic mechanism and a possible BPA degradation pathway during this oxidation process will be elucidated in detail.

2. Materials and methods

2.1. Catalysts fabrication

2.1.1. Synthesis of ultrathin $BiO(HCOO)_xI_{1-x}$ composite nanosheets

The ultrathin $BiO(HCOO)_xI_{1-x}$ nanosheets were prepared via a simple solvothermal method. Typically, 0.972 g $Bi(NO_3)_3{\cdot}5H_2O$ and 0.8 g PVP were added to 60 mL glycerol solution (glycerol: water = 1:1) with stirring for 30 min at room temperature. 5 mL solution with different proportions of HCOONa and KI (total mole of 2.0 mmol) were dropped into the above mixture with further 30 min stirring. Subsequently, the mixture was transferred to a 100 mL Teflon-lined stainless steel autoclave and heated at 160 °C for 6 h. Finally, the finished product was collected after centrifugation, washed three times with water and dried at 50 °C. The obtained sample is recorded as BHI-x, where x is the molar ratio of HCOONa to the sum of HCOONa and KI (x = 0, 0.25, 0.50, 0.65, 0.75, 0.85 and 1), abbreviated as BI, BHI-0.25, BHI-0.50, BHI-0.65, BHI-0.75, BHI-0.85, BH.

2.1.2. Synthesis of $BiO(HCOO)_xI_{1-x}$ nanoplate composites

For comparison, the BHI-0.75 nanoplates were prepared via a similar method without adding PVP, which was named as BHI-P (Text S1).

2.2. Photocatalytic activity measurement

A 300 W xenon lamp source (Beijing Perfectlight, PLS-SXE300D) with a 420 nm cut-off filter was employed as the light source, and the emission spectrum was displayed in Fig. S1. In a typical photocatalytic degradation experiment, 50 mg of sample was added into 100 mL of targeted contaminant solution (5 mg/L). Before the irradiation experiment, the dark experiments were conducted to get the adsorption equilibrium. The temperature of the reaction system was kept at 25 °C by continuous circulating water. The illumination intensity of the reactor was stabilized at 1.288 W. At certain time intervals, 2 mL of the reaction solution was taken out and filtrated via a filter (0.45 μm) to

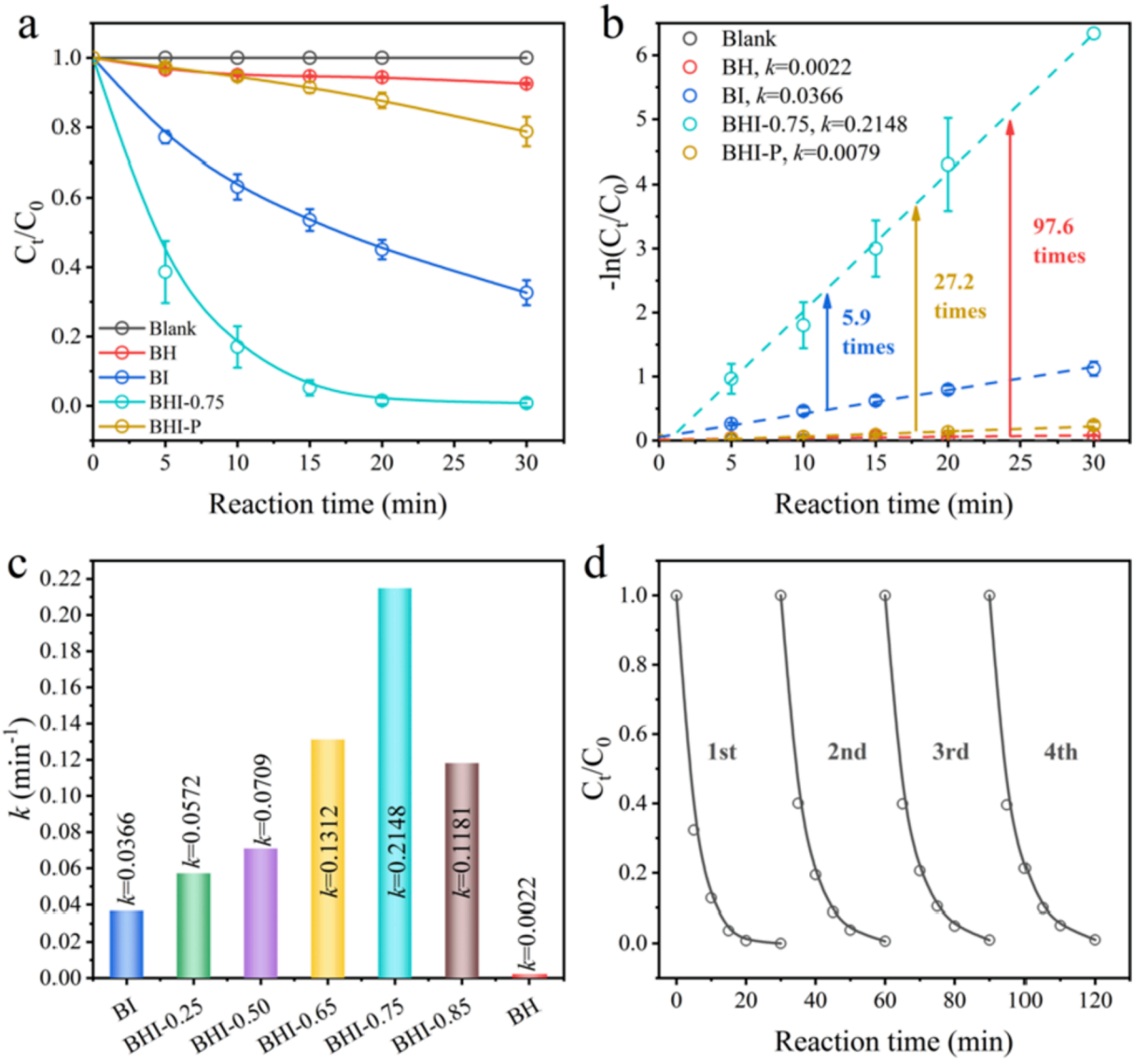

Fig. 4. (a) BPA removal curves under VL irradiation with different photocatalysts, (b) the corresponding kinetic fitting curves, (c) the apparent rate constants of BHI-x samples in BPA degradation, and (d) the reusability test of BPA degradation in the BHI-0.75/VL system.

determine the residual concentration of contaminants. The concentration of targeted contaminants were analyzed by the UPLC system (Waters, ACQUITY UPLC H-CLASS) with a BEH-C18 column. More detailed information about the chemicals, characterization, analytical methods and experimental processes were shown in Supporting Information.

3. Results and discussion

3.1. Characteristics

The crystalline structures of the $BiO(HCOO)_xI_{1-x}$ composites with different x values were characterized by XRD analysis. As shown in Fig. 1a, peaks of prepared pure BiOCOOH (x = 1) and BiOI (x = 0) match well with the standard diffraction peaks of tetragonal BiOCOOH (PDF#35–0939) and BiOI (PDF#10–0445), respectively. Specially, in Fig. 1b, with the additive amount of I increases, the intensity of diffraction peak at $2\theta = 29.6^\circ$ and 31.6° are enhanced, which index to the (1 0 2) and (1 1 0) facets of BiOI. Therefore, it can be demonstrated that as-prepared $BiO(HCOO)_xI_{1-x}$ composites were hybrid intermediary combining BiOCOOH and BiOI, rather than solid solution.

The morphologies of photocatalysts were depicted in Fig. 2. SEM images (Fig. 2a-b) clearly present the rod-like and sheet-like structures of BH and BI, respectively. Noteworthily, the BHI-0.75 also exhibits a stacked sheet-like structure (Fig. 2c), indicating that the introduction of I element to BiOCOOH crystals change the sample morphology from nanorods to nanosheets. Fig. 2d are the corresponding SEM-EDS mapping images of BHI-0.75, demonstrating that Bi, O, C and I elements are evenly distributed over the composite. In Fig. 2e-f, the TEM images further indicate the cumulate nanosheet structure of BHI-0.75 with the side-face thickness of average 2.85 nm, verifying the as-prepared BHI-0.75 sample belongs to the ultrathin nanosheet structure. Meanwhile, the well crystallized and clear lattice fringes with the d-spacing of 0.266 nm, 0.282 nm and 0.301 nm are observed in the corresponding high-magnification of TEM image (Fig. 2g), which can be indexed to the (1 1 1), (1 1 0) and (1 0 2) planes of tetragonal BHI-0.75, respectively [18,33]. Furthermore, the thickness of BHI-0.75 nanosheet is accurately measured to be ~2.47 nm via AFM test (Fig. 2h-i), which is in accordance with the TEM results. In contrast, the thickness of BHI-P nanoplate (control sample) is determined to be 6.26 nm (Fig. S2), which is about three folds than that of BHI-0.75. The above results sufficiently manifested that the 2D ultrathin $BiO(HCOO)_xI_{1-x}$ composite nanosheets were successfully synthesized.

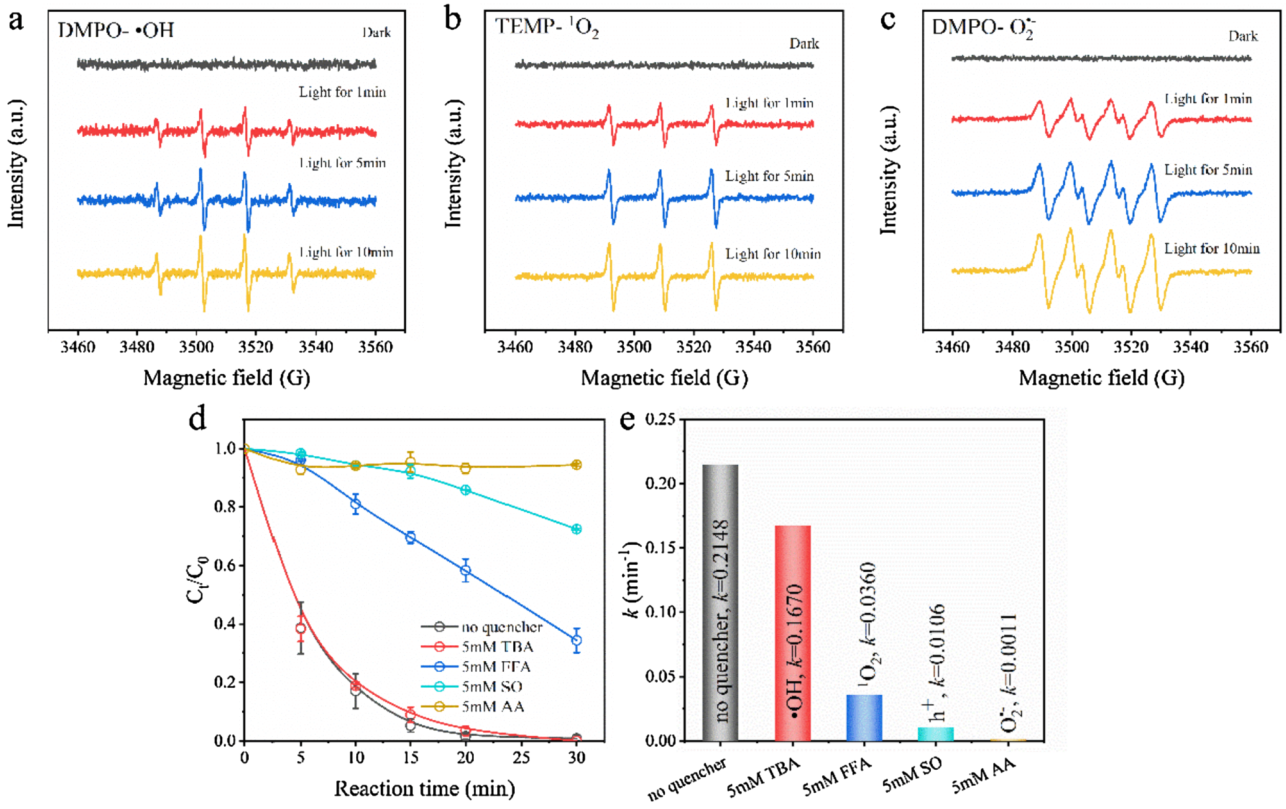

Fig. 5. (a) The ESR spectra of DMPO-·OH, (b) TEMP-$^1O_2$ and (c) DMPO-$O_2^{\bullet-}$ in the BHI-0.75/VL system at different time, (d) radical screening experiments in BHI-0.75/VL system and (e) the corresponding kinetic constant (k) values.

The surface elemental chemical states of photocatalysts were investigated by XPS measurement. Fig. 3a displays the survey spectra of ultrathin BHI-0.75 and BHI-P, which clearly depicts that the Bi, I, C and O elements are involved in these two samples. In Fig. 3b, the peak values of Bi $4f_{5/2}$ and Bi $4f_{7/2}$ are 164.12 eV and 158.78 eV, respectively, which can be classified to the characteristic of Bi^{3+} of bismuth oxide materials [34,35]. The BHI-0.75 peaks in I 3d spectra locate at 618.6 eV and 630.1 eV, attributed to I $3d_{5/2}$ and I $3d_{3/2}$, respectively, and BHI-P exhibits two similar peaks at 618.8 eV and 630.4 eV (Fig. 3c). It is further elucidate the successfully introduction of I element to these samples [36,37]. In Fig. 3d, the C1s spectrum is divided into two peaks of 285.0 eV and 287.6 eV, deemed as C-C binding and carboxyl group, respectively [38]. And three peaks at 529.5 eV, 530.9 eV and 532.4 eV in the O 1 s spectra (Fig. 3e) can be ascribed to Bi-O, O-H and –COOH, respectively [34,39]. These above analysis indicated that the as-prepared ultrathin BHI-0.75 nanosheets and BHI-P nanoplates were both hybrid composite structure and there was no obvious difference between their surface chemical composition.

3.2. Photocatalytic activity

For evaluating the visible-light (VL) photocatalytic performance of different samples, BPA was adopted as a probe contaminant and the results were displayed in Fig. 4. As displayed in Fig. S3a, the reaction system can reach the absorption-desorption equilibrium within 15 min under dark condition, and there is less than 10% BPA adsorption to all the samples, revealing that the adsorption effect is very weak. In Fig. 4a, the BPA itself shows scarcely any decomposition without photocatalyst. After adding photocatalysts, the BPA removal efficiencies over BH and BI are 7.5% and 67.4%, respectively, while the ultrathin BHI-0.75 reaches up to 100% removal within 30 min VL irradiation, suggesting that the hybrid structure makes a remarkable contribution to enhance the photocatalytic activity of samples. Meanwhile, it is worth noting that the degradation rate of BHI-0.75 is significantly greater than that of BHI-P (only 21.3%), even though the ratio of I to COOH are the same in these two hybrid composites. Considering the similar chemical composition and different thickness between BHI-0.75 and BHI-P, it can be concluded that the 2D ultrathin structure is another beneficial factor for the boosted oxidation activity of BHI-0.75. In addition, the change of total organic carbon (TOC) in several reaction systems was explored. As presented in Fig. S4, the TOC removal efficiency within 30 min of BHI-0.75/VL system (17.9%) is much higher than that of BH/VL (0.9%), BI/VL (7.6%) and BHI-P/VL (2.1%) systems, further manifesting the excellent photocatalytic performance of BHI-0.75. Moreover, compared to other Bi-based materials (Table S2) and several common semiconductor materials (Table S3) previously reported, the 2D ultrathin BHI-x composite nanosheets exhibited a relatively rapid BPA degradation or high degradation efficiency under visible light irradiation.

Moreover, the BPA degradation in all systems follows well the pseudo first-order model. The kinetic rate (k) of BHI-0.75 is 0.2148 min^{-1}, which increases by 5.9, 27.2 and 97.6 folds with respect to that of BI (k = 0.0366 min^{-1}), BHI-P (k = 0.0079 min^{-1}) and BH (k = 0.0022 min^{-1}), respectively (Fig. 4b). Fig. 4c and Fig. S3b display the photocatalytic activity over BHI-x composite nanosheets (x = 1, 0.85, 0.75, 0.65, 0.50, 0.25 and 0). Clearly, it can be seen that as the COOH content in BHI-x increases, the k value raises initially and then reduces, among which the maximum k is achieved at x = 0.75. Besides, the recyclability of ultrathin BHI-0.75 nanosheets during BPA degradation was also investigated. In Fig. 4d, recycle experiments on BHI-0.75 show that 99.0% BPA degradation efficiency can be still achieved after repeated use of four cycles and the k value decreases slightly from 0.2148 min^{-1} (1st cycle) to 0.1489 min^{-1} (4th cycle). The Bi^{3+} leakage is measured to be 35.3 μg/L after degradation, which satisfies the water quality safety standard (GB5749-2006). And there is no obvious change between the XRD patterns of fresh and 4th repeated BHI-0.75 (Fig. S5), manifesting that the reusability and stability of BHI-0.75 are fairly superior. In

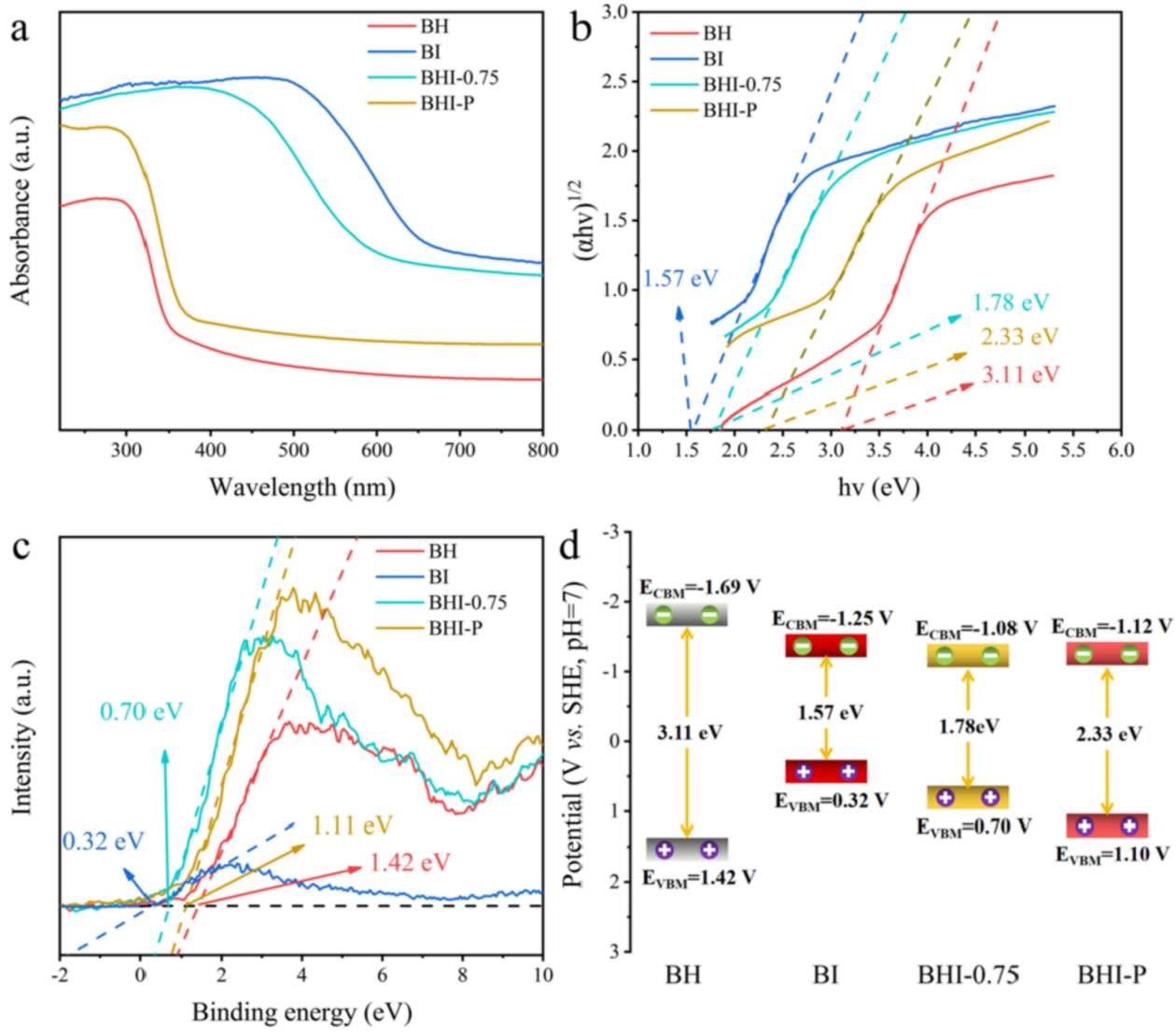

Fig. 6. (a) UV–Vis DRS, (b) $(\alpha h\nu)^{1/2}$-$h\nu$ relation curve, and (c) VB-XPS spectra of different samples. (d) The energy band diagram.

addition, as shown in Fig. S6, sulfamethazine (SMT), bisphenol F (BPF) and 4-hydroxybenzoic acid (4-HBA) are able to be eliminated in the BHI-0.75/VL system with the removal efficiency of 99%, 99% and 74%, respectively, suggesting the universal oxidizing ability of this system.

3.3. Photocatalytic oxidation mechanism

3.3.1. Identification of reactive species

In situ ESR measurements were conducted to shed light on the reactive species involved in the reaction system. Based on Fig. 5a-c, there were no definable ESR signals found without light. In contrast, the signals of DMPO-·OH, DMPO-$O_2^{\bullet-}$ and TEMP-$^1O_2$ adducts were discovered under VL irradiation, and the signal intensity of all reactive oxygen species (ROS) strengthened with time prolonged, revealing that ·OH, $O_2^{\bullet-}$ and $^1O_2$ are all generated in the BHI-0.75/VL system. Furthermore, to elucidate the contribution of different ROS to BPA degradation, the quenching experiments were performed, where the tert-butyl alcohol (TBA), ascorbic acid (AA), Furfuryl alcohol (FFA) and sodium oxalate (SO) were selected as the scavengers of ·OH [40], $O_2^{\bullet-}$ [41], $^1O_2$ [42] and h^+ [41]. Fig. 5d-e disclose that when TBA and FFA are added into the oxidation system, the kinetic constants (k) decline from 0.2148 to 0.1670 and 0.0306 min^{-1}, respectively. Nonetheless, when the AA and SO are introduced to the system, the BPA elimination are significantly inhibited, in which the k values decrease to 0.0011 and 0.0101 min^{-1}, respectively. All above results indicate that the $O_2^{\bullet-}$ and h^+ play a crucial role in the BHI-0.75/VL system for BPA degradation, and the contribution of $^1O_2$ and ·OH is secondary, which follow the order of $O_2^{\bullet-}$ > h^+ > $^1O_2$ > ·OH.

3.3.2. Relationship between photoelectric property and photocatalytic activity

Given the superior photocatalytic activity of ultrathin BHI-0.75 nanosheet, a series of characterizations were conducted to reveal its origin. Firstly, the optical properties and band parameters of as-prepared samples were investigated by UV–vis DRS and VB-XPS measurements. According to Fig. 6a, the absorption edges of BHI-0.75 and BHI-P both have a significant red-shifting in comparison with BH, but lower than that of BI, indicating that the hybridization structure could tune the VL absorption ability, which is in accordance with the previous studies [43,44]. Noteworthily, the VL absorption of BHI-0.75 enhances distinctly when compared with BHI-P, demonstrating that the 2D ultrathin structure will be conducive to improve the optical absorption [45,46]. According to the Tauc plots, the band gap energy of BH, BI, BHI-0.75 and BHI-P are ascertained at 3.11, 1.57, 1.78 and 2.33 eV, respectively (Fig. 6b). Meanwhile, from the VB-XPS, the valence band maximum (E_{VBM}) positions are confirmed at 1.42, 0.32, 0.70 and 1.11

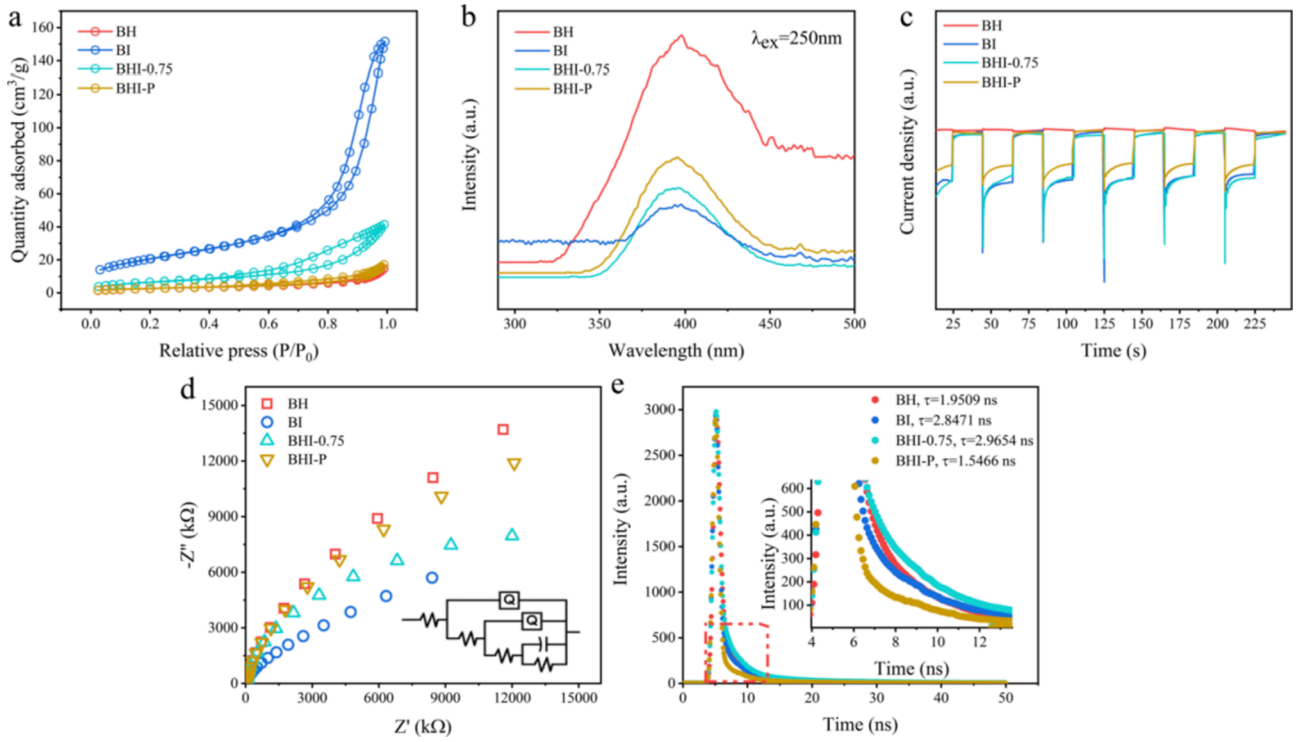

Fig. 7. (a) N_2 adsorption–desorption isotherms, (b) PL spectra, (c) transient photocurrent responses, (d) EIS spectra and (e) time-resolved PL spectra of the photocatalysts.

Table 1
Normalization of the kinetic rates of the catalysts.

Samples	k ($\times 10^{-3}$ min^{-1})	A_s (m^2·g^{-1})	k_n ($\times 10^{-3}$ min^{-1}·L·m^{-2})
BH	0.0022	9.684	0.0454
BI	0.0366	75.490	0.0970
BHI-0.75	0.2148	23.291	1.8445
BHI-P	0.0079	9.731	0.1624

eV for BH, BI, BHI-0.75 and BHI-P samples, respectively (Fig. 6c). Based on the formular of $E_{CBM} = E_{VBM}$ - Eg, the conduction band minimum (E_{CBM}) potentials of BH, BI, BHI-0.75 and BHI-P are −1.69, −1.25, −1.08 and −1.12 eV, respectively. Taken together, the energy band of four photocatalysts are diagrammed in Fig. 6d. Obviously, for the ultrathin BHI-0.75 hybrid composite, the band gap is narrower than that of BH and BHI-P, and the VBM position is higher than that of BI, demonstrating that BHI-0.75 possesses an enhanced VL absorption ability and elevated oxidation driving force simultaneously. Therefore, the fabrication of ultrathin hybrid composite devotes to achieve the balance of the VL absorption capability and oxidizing ability of h^+ to a certain degree, which is very likely to induce the remarkable photocatalytic performance of BHI-0.75.

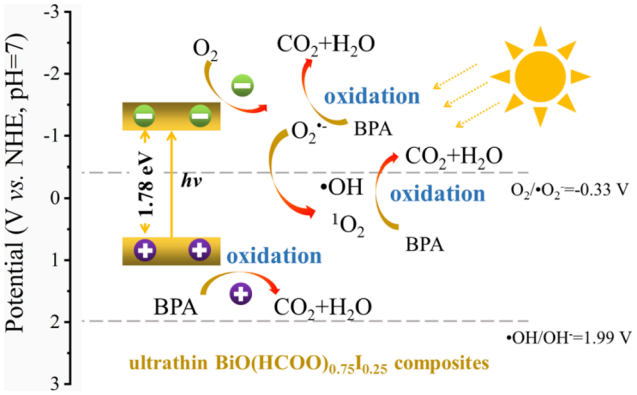

Fig. 8. Photo-oxidation mechanism schematic in BHI-0.75/VL system.

Secondly, the N_2 adsorption-desorption isotherm of BH, BI, BHI-0.75 and BHI-P samples were measured to verify the contribution of surface area (Fig. 7a). The surface area of BH, BI, BHI-0.75 and BHI-P are calculated to be 9.731, 75.490, 23.291 and 9.684 m^2·g^{-1}, respectively. Based on these, normalize the kinetic constant (k) through surface area (A_s) and catalyst concentration (C) and herein define it as:

$$K_n = \frac{K}{C \times A_s} \quad (1)$$

As depicted in Table 1, after excluding the influence of surface area, BHI-0.75 exhibits the highest k_n (1.8445×10^{-3} min^{-1}·L·m^{-2}), which is 40.6, 11.4 and 19.0 folds than that of BH, BHI-P, and BI, respectively. As a result, the surface area would seldom attribute to the preeminent photocatalytic activity of BHI-0.75.

Subsequently, the photoelectric performance curves were recorded to unveil the separation and migration peculiarity of photogenerated carriers. As shown in Fig. 7b, the photoluminescence (PL) intensity of BHI-0.75 quenches obviously compared with BH and keeps close to BI, demonstrating that the hybrid structure would favor to carrier separation [47,48]. Moreover, the PL intensity of BHI-0.75 takes on a further weaken with respect to BHI-P, manifesting that ultrathin structure could further accelerate the separation of photoinduced carriers. Likewise, the transient photocurrent response (Fig. 7c) and electrochemical impedance spectroscopy (EIS, Fig. 7d) of the samples display the similar tendency with PL spectra. Combining the equivalent circuit model, the charge transfer resistance (R_{ct}) of the photocatalysts are fitted and listed in Table S4. The BHI-0.75 sample possesses the smaller resistance by more than an order of magnitude than other control samples, suggesting its high carrier mobility. In addition, the time-resolved photoluminescence (TRPL) were detected to explore the charge carrier lifetime. It can be clearly seen from Fig. 7e that the BHI-0.75 nanosheets

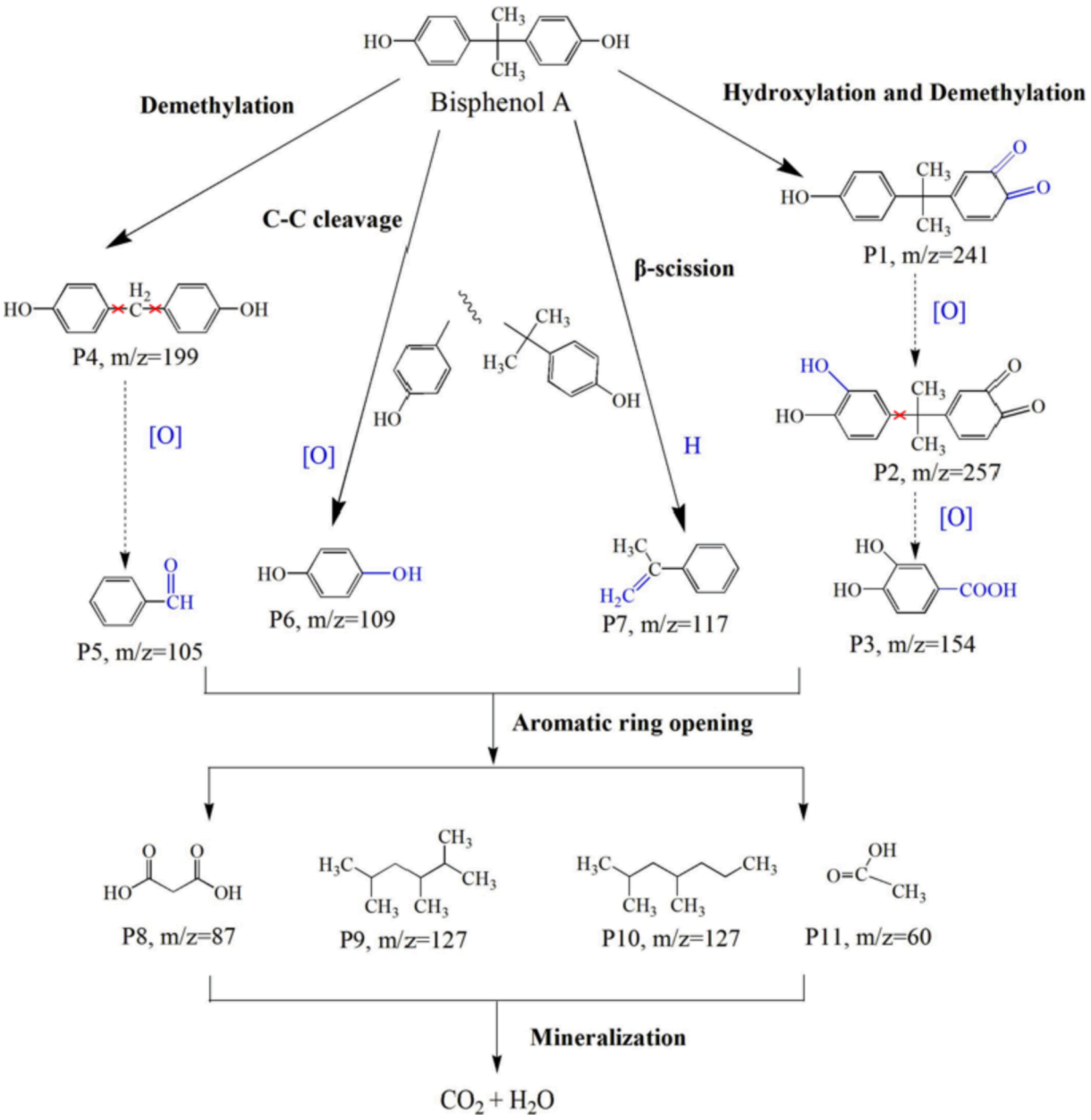

Fig. 9. The degradation pathways of BPA in the BHI-0.75/VL system.

exhibit the longest lifetime with 2.9654 ns, which is much longer than that of BH (1.9509 ns), BI (2.8471 ns) and BHI-P (1.5466 ns), respectively. The above outcomes indicate that the synergistic effect of hybrid composite and ultrathin structure is able to promote the separation rate of photoinduced charge carrier, which should greatly prolong the carriers lifetime and benefit the photocatalytic reaction [49].

Therefore, combining the above analyses of ROS and photoelectric property, the photocatalytic oxidation mechanism of BHI-0.75/VL system can be summarized as follows. On one hand, the hybrid composite can regulate the electronic structure, which efficiently narrows the band gap to adsorb more VL radiation, endows a strong oxidizing h^+ via relative high VB position, and restrains the photoinduced charge recombination. On the other hand, the ultrathin structure can expand the VL adsorption capacity, together with enhancing the separation of charges by the rapid migration to the catalytic interface. Thus, the photocatalytic activity of BHI-0.75 is improved with the synergistic effect of the two aspects. As displayed in Fig. 8, when the light hits the surface of BHI-0.75, the photoinduced electrons (e^-) are motivated and transferred to the CB, while the photoinduced holes (h^+) are retained in VB. Since the VBM position of BHI-0.75 is below E(·OH/OH^-) (1.99 V *vs.* SHE), the h^+ is incapable of oxidizing the adsorbent H_2O molecules to produce ·OH. Instead, the h^+ of VB possesses a relevant strong oxidizing ability to eliminate organic matters directly. Owing to the CBM position of BHI-0.75 locates much negative than E($O_2/O_2^{\bullet-}$) (-0.33 V *vs.* SHE), the dissolved oxygen can react with e^- to generate vast $O_2^{\bullet-}$, and then $^1O_2$ and ·OH are also produced via the conversion of part of $O_2^{\bullet-}$. Thereby, the multiple ROS, including $O_2^{\bullet-}$, h^+, $^1O_2$ and ·OH, are generated continuously in the BHI-0.75/VL system, which can decompose BPA into CO_2 and H_2O effectively.

To further reveal the BPA transformation process in BHI-0.75/VL system, eleven oxidation intermediates were identified from LC-MS/MS spectra (Fig. S7-S17 and Table S5), and the relevant degradation pathways of BPA have been proposed in Fig. 9. There are four degradation pathways existing in the BHI-0.75/VL system, including (i) hydroxylation and demethylation, (ii) C-C cleavage, (iii) β–scission reaction, and (iv) polymerization. Detailedly, the ROSs usually attack

the ortho position in the aromatic ring of BPA, which should be transformed to P1 via hydroxylation and further dehydrogenation reaction [50]. Along with the hydroxylation reaction continues, P1 is further oxidized to P2 and P3 by C-C cleavage. Meanwhile, in another demethylation pathway, the BPA may be dehydrogenized directly to generate P4, which is subsequently transferred to P5 [51]. BPA also can be eliminated via C-C cleavage and β–scission reaction to produce P6 and P7, respectively [52]. Thereafter, these BPA intermediates can be further oxidized to P8, P9, P10 and P11 via opening the aromatic rings, and at last all of products are mineralized into carbon dioxide and water by massive ROS.

4. Conclusion

Here, a 2D ultrathin $BiO(HCOO)_xI_{1-x}$ composite photocatalytic system was put forward as a novel and valid strategy to eliminate BPA. As an optimal ratio of $BiO(HCOO)_{0.75}I_{0.25}$, BPA could be entirely removed within 30 min irradiation, and the rate constant increased by 5.9, 97.6 and 27.2 folds when compared with BiOI, BiOCOOH and $BiO(HCOO)_{0.75}I_{0.25}$-P nanoplates, respectively. Based on multiplied optical and photoelectric experiments, the synergistic effect between ultrathin morphology and hybrid structure was verified, which endowed $BiO(HCOO)_xI_{1-x}$ nanosheet a high VBM position, a broad VL adsorption range, and an efficient photogenerated charges separation rate, leading to its remarkable photocatalytic performance. Radical screening experiment uncovered that the $O_2^{\bullet-}$ and h^+ played a crucial role, while $^1O_2$ and ·OH made the secondary contribution in $BiO(HCOO)_xI_{1-x}$/VL system. Additionally, the possibly BPA transformation routes were proposed. We believe that such ultrathin hybrid strategy will provide a broad prospect for promoting photocatalysis, and it is hopeful to show its capabilities in other fields, such as supercapacitor and electrocatalysis.

CRediT authorship contribution statement

Qiao Wang: Methodology, Validation, Formal analysis, Writing – original draft, Funding acquisition. **Guanheng Lv:** Investigation, Data curation, Writing – original draft, Visualization. **Yiting Cao:** Investigation, Data curation. **Zhenhui Chen:** Investigation, Data curation. **Jialin Jia:** Conceptualization, Methodology, Supervision, Writing – review & editing. **Yanlin Qin:** Conceptualization, Methodology, Supervision. **Zhenxuan Lin:** Investigation, Data curation. **Xuan Xie:** Investigation, Data curation. **Zhihong Wang:** Writing – review & editing.

Declaration of Competing Interest

The authors declare that they have no known competing financial interests or personal relationships that could have appeared to influence the work reported in this paper.

Acknowledgements

The authors gratefully acknowledge the National Natural Science Foundation of China (Grant No. 22006022), the Open Project of State Key Laboratory of Urban Water Resource and Environment (Grant No. HC202154), and Guangzhou Basic and Applied Basic Research Foundation (Grant No. 202102020348).

Appendix A. Supplementary material

Supplementary data to this article can be found online at https://doi.org/10.1016/j.seppur.2021.120153.

References

[1] T.K. Kasonga, M.A.A. Coetzee, I. Kamika, V.M. Ngole-Jeme, M.N.B. Momba, Endocrine-disruptive chemicals as contaminants of emerging concern in wastewater and surface water: a review, J. Environ. Manage. 277 (2021), 111485.
[2] T. Filardi, F. Panimolle, A. Lenzi, S. Morano, Bisphenol A and phthalates in diet: an emerging link with pregnancy complications, Nutrients 12 (2020) 525.
[3] Z.H. Liu, Z. Dang, H. Yin, Y. Liu, Making waves: improving removal performance of conventional wastewater treatment plants on endocrine disrupting compounds (EDCs): their conjugates matter, Water Res. 188 (2021), 116469.
[4] M.J. Fang, C.W. Tsao, Y.J. Hsu, Semiconductor nanoheterostructures for photoconversion applications, J. Phys. D: Appl. Phys. 53 (2020), 143001.
[5] Z.Q. Long, Q.G. Li, T. Wei, G.M. Zhang, Z.J. Ren, Historical development and prospects of photocatalysts for pollutant removal in water, J. Hazard. Mater. 395 (2020), 122599.
[6] C. Zhang, Y.i. Li, D. Shuai, Y. Shen, W. Xiong, L. Wang, Graphitic carbon nitride (g-C_3N_4)-based photocatalysts for water disinfection and microbial control: a review, Chemosphere 214 (2019) 462–479.
[7] X. Xu, X. Ding, X.L. Yang, P. Wang, S. Li, Z.X. Lu, H. Chen, Oxygen vacancy boosted photocatalytic decomposition of ciprofloxacin over Bi_2MoO_6: oxygen vacancy engineering, biotoxicity evaluation and mechanism study, J. Hazard. Mater. 364 (2019) 691–699.
[8] G.A. Jie, B. Chsa, S.A. Jie, A. Xjx, A. Xyl, A. Zhf, A. Ztl, A. Xjw, Highly efficient activation of peroxymonosulfate by Co_3O_4/Bi_2MoO_6 p-n heterostructure composites for the degradation of norfloxacin under visible light irradiation - ScienceDirect, Sep. Purif. Technol. 259 (2020), 118109.
[9] Y.L. Wang, K. Ding, R. Xu, D. Yu, W. Wang, P. Gao, B.J. Liu, Fabrication of $BiVO_4$/$BiPO_4$/GO composite photocatalytic material for the visible light-driven degradation, J. Clean. Prod. 247 (2020), 119108.
[10] C. Sha, B. Dha, B. Gza, B. Wxa, L. Lei, B. Pxa, D. Rui, L. Jing, C. Min, In-situ synthesis of facet-dependent $BiVO_4$ /Ag_3PO_4 /PANI photocatalyst with enhanced visible-light-induced photocatalytic degradation performance: synergism of interfacial coupling and hole-transfer, Chem. Eng. J. 382 (2020) 122840–122840.
[11] H. Zhang, J. He, C. Zhai, M. Zhu, 2D Bi_2WO_6/MoS_2 as a new photo-activated carrier for boosting electrocatalytic methanol oxidation with visible light illumination, Chin. Chem. Lett. 30 (12) (2019) 2338–2342.
[12] Y. Yan, H. Yang, Z. Yi, X. Wang, R. Li, T. Xian, Evolution of Bi nanowires from BiOBr nanoplates through a $NaBH_4$ reduction method with enhanced photodegradation performance, Environ. Eng. Sci. 37 (1) (2020) 64–77.
[13] C. Ma, J. Wei, K. Jiang, Z. Yang, X. Yang, K. Yang, Y. Zhang, C. Zhang, Self-assembled micro-flowers of ultrathin Au/BiOCOOH nanosheets photocatalytic degradation of tetracycline hydrochloride and reduction of CO_2, Chemosphere 283 (2021), 131228.
[14] M. Hao, T. Yi, Y. Cao, Y. Song, Z. Cao, W. He, Y. Gao, J. Liu, Enhanced visible light photocatalytic activity in AgI/BiOCOOH composite, Adv. Powder Technol. 30 (1) (2019) 111–119.
[15] L. Yang, Q. Han, X. Wang, J. Zhu, Highly efficient removal of aqueous chromate and organic dyes by ultralong HCOOBiO nanowires, Chem. Eng. J. 262 (2015) 169–178.
[16] S.-H. Xia, C. Dong, X.-W. Wei, J. Wang, K.-L. Wu, Y.u. Hu, Y. Ye, Reduced graphene oxide modified flower-like BiOCOOH architectures with enhanced photocatalytic activity, Mater. Lett. 156 (2015) 36–38.
[17] S.J. Li, B. Xue, G.Y. Wu, Y.P. Liu, H.Q. Zhang, D.Y. Ma, J.C. Zuo, A novel flower-like Ag/AgCl/BiOCOOH ternary heterojunction photocatalyst: facile construction and its superior photocatalytic performance for the removal of toxic pollutants, Nanomaterials 9 (2019) 1562.
[18] Q. Wang, Z. Liu, D. Liu, G. Liu, M. Yang, F. Cui, W. Wang, Ultrathin two-dimensional $BiOBr_xI_{1-x}$ solid solution with rich oxygen vacancies for enhanced visible-light-driven photoactivity in environmental remediation, Appl. Catal. B 236 (2018) 222–232.
[19] R. Shen, Y. Ding, S. Li, P. Zhang, Q. Xiang, Y.H. Ng, X. Li, Constructing low-cost Ni_3C/twin-crystal $Zn_{0.5}Cd_{0.5}S$ heterojunction/homojunction nanohybrids for efficient photocatalytic H_2 evolution, Chinese, J. Catal. 42 (1) (2021) 25–36.
[20] Y. Xie, D. Liu, B. Wang, D. Li, Z. Yan, Y. Chen, J. Shen, Z. Zhang, X. Wang, Monolayer $Bi_2W_{1-x}Mo_xO_6$ solid solutions for structural polarity to boost photocatalytic reduction of nitrobenzene under visible light, ACS Sustain. Chem. Eng. 9 (6) (2021) 2465–2474.
[21] H.-B. Huang, K. Yu, N. Zhang, J.-Y. Xu, X.-T. Yu, H.-X. Liu, H.-L. Cao, J. Lü, R. Cao, Localized surface plasmon resonance enhanced visible-light-driven CO_2 photoreduction in Cu nanoparticle loaded ZnInS solid solutions, Nanoscale 12 (28) (2020) 15169–15174.
[22] J. Li, W. Yang, A. Wu, X. Zhang, T. Xu, B. Liu, Band-gap tunable 2D hexagonal $(GaN)_{1-x}(ZnO)_x$ solid-solution nanosheets for photocatalytic water splitting, ACS Appl. Mater. Interfaces 12 (7) (2020) 8583–8591.
[23] M. Yadav, S. Garg, A. Chandra, K. Hernadi, Fabrication of leaf extract mediated bismuth oxybromide/oxyiodide ($BiOBr_xI_{1-x}$) photocatalysts with tunable band gap and enhanced optical absorption for degradation of organic pollutants, J. Colloid Interface Sci. 555 (2019) 304–314.
[24] W. Jiang, Z. Li, C. Liu, D. Wang, G. Che, Enhanced visible-light-induced photocatalytic degradation of tetracycline using BiOI/MIL-125(Ti) composite photocatalyst, J. Alloys Compd. 854 (2021), 157166.
[25] Y.-R. Jiang, H.-P. Lin, W.-H. Chung, Y.-M. Dai, W.-Y. Lin, C.-C. Chen, Controlled hydrothermal synthesis of BiO_xCl_y/BiO_mI_n composites exhibiting visible-light photocatalytic degradation of crystal violet, J. Hazard. Mater. 283 (2015) 787–805.

[26] H. Wang, H. Yuan, S. Sae Hong, Y. Li, Y.i. Cui, Physical and chemical tuning of two-dimensional transition metal dichalcogenides, Chem. Soc. Rev. 44 (9) (2015) 2664–2680.
[27] F. Bonaccorso, L. Colombo, G.H. Yu, M. Stoller, V. Tozzini, A.C. Ferrari, R.S. Ruoff, V. Pellegrini, Graphene, related two-dimensional crystals, and hybrid systems for energy conversion and storage, Science 347 (2015), 146501.
[28] M. Nasilowski, B. Mahler, E. Lhuillier, S. Ithurria, B. Dubertret, Two-dimensional colloidal nanocrystals, Chem. Rev. 116 (18) (2016) 10934–10982.
[29] C.L. Tan, H. Zhang, Wet-chemical synthesis and applications of non-layer structured two-dimensional nanomaterials, Nat. Commun. 6 (2015) 1–13.
[30] C. Tan, X. Cao, X.-J. Wu, Q. He, J. Yang, X. Zhang, J. Chen, W. Zhao, S. Han, G.-H. Nam, M. Sindoro, H. Zhang, Recent advances in ultrathin two-dimensional nanomaterials, Chem. Rev. 117 (9) (2017) 6225–6331.
[31] Y. Sun, S. Gao, F. Lei, Y.i. Xie, Atomically-thin two-dimensional sheets for understanding active sites in catalysis, Chem. Soc. Rev. 44 (3) (2015) 623–636.
[32] J. Di, J. Xiong, H. Li, Z. Liu, Ultrathin 2D photocatalysts: Electronic-structure tailoring, hybridization, and applications, Adv. Mater. 30 (2018) 1704548.
[33] Y. Cui, X. Zhang, H. Zhang, Q. Cheng, X. Cheng, Construction of BiOCOOH/g-C_3N_4 composite photocatalyst and its enhanced visible light photocatalytic degradation of amido black 10B, Sep. Purif. Technol. 210 (2019) 125–134.
[34] P. Chen, Q. Zhang, Y. Su, L. Shen, F. Wang, H. Liu, Y. Liu, Z. Cai, W. Lv, G. Liu, Accelerated photocatalytic degradation of diclofenac by a novel CQDs/BiOCOOH hybrid material under visible-light irradiation: dechloridation, detoxicity, and a new superoxide radical model study, Chem. Eng. J. 332 (2018) 737–748.
[35] X. Meng, X. Cheng, D. Zhuang, S. Yang, C. Sun, Preparation of Ag_3PO_4/BiOCOOH composite photocatalysts with high photocatalytic performances under visible light irradiation, NANO 11 (2016) 1650105.
[36] X. Li, T. Chen, H. Lin, J. Cao, H. Huang, S. Chen, Intensive photocatalytic activity enhancement of Bi_5O_7I via coupling with band structure and content adjustable $BiOBr_xI_{1-x}$, Sci. Bull. 63 (4) (2018) 219–227.
[37] H. Liu, H. Zhang, M. Chen, C. Zhang, C. Du, J. Peng, K. Jiang, Peroxymonosulfate-assisted photocatalysis with g-C_3N_4 /BiOCOOH nanocomposites for the synergistic removal of organic pollutants, J. Water Process. Eng. 38 (2020), 101580.
[38] C. Liang, H.P. Feng, H.Y. Niu, C.G. Niu, J.S. Li, D.W. Huang, L. Zhang, H. Guo, N. Tang, H.Y. Liu, A dual transfer strategy for boosting reactive oxygen species generation in ultrathin Z-scheme heterojunction driven by electronic field, Chem. Eng. J. 384 (2020), 123236.
[39] Y. Chen, X. Ji, S. Vadivel, B. Saravanakumar, Low-cost fabrication of BiOCOOH microflowers for high-performance supercapacitors applications, J. Mater. Sci. Mater. Electron. 30 (9) (2019) 8903–8910.
[40] E. Saputra, S. Muhammad, H. Sun, H.-M. Ang, M.O. Tadé, S. Wang, Shape-controlled activation of peroxymonosulfate by single crystal α-Mn_2O_3 for catalytic phenol degradation in aqueous solution, Appl. Catal. B 154-155 (2014) 246–251.
[41] Q. Wang, W. Wang, L. Zhong, D. Liu, X. Cao, F. Cui, Oxygen vacancy-rich 2D/2D BiOCl-g-C_3N_4 ultrathin heterostructure nanosheets for enhanced visible-light-driven photocatalytic activity in environmental remediation, Appl. Catal. B 220 (2018) 290–302.
[42] E.T. Yun, J.H. Lee, J. Kim, H.D. Park, J. Lee, Identifying the nonradical mechanism in the peroxymonosulfate activation process: singlet oxygenation versus mediated electron transfer, Environ. Sci. Technol. 52 (2018) 7032–7042.
[43] X. Zhang, L.-W. Wang, C.-Y. Wang, W.-K. Wang, Y.-L. Chen, Y.-X. Huang, W.-W. Li, Y.-J. Feng, H.-Q. Yu, Synthesis of $BiOCl_xBr_{1-x}$ nanoplate solid solutions as a robust photocatalyst with tunable band structure, Chemistry 21 (33) (2015) 11872–11877.
[44] Y. Bai, L. Ye, T. Chen, P. Wang, L.i. Wang, X. Shi, P.K. Wong, Synthesis of hierarchical bismuth-rich $Bi_4O_5BrxI_{2-x}$ solid solutions for enhanced photocatalytic activities of CO_2 conversion and Cr(VI) reduction under visible light, Appl. Catal. B 203 (2017) 633–640.
[45] L. Wang, L. Zan, Band-gap-energy-adjustable and noble-metal-free modified NiS-$Zn_xCd_{1-x}S$ for highly efficient visible-light-driven Cr^{6+} photoreduction in alkaline wastewater, J. Phys. Chem. Solids 150 (2021), 109893.
[46] A. Yh, W. Kai, A. Tg, C. Jl, A. Xw, G. D Construction of 2D/2D Bi_2Se_3/g-C_3N_4 nanocomposite with High interfacial charge separation and photo-heat conversion efficiency for selective photocatalytic CO_2 reduction - ScienceDirect, Appl. Catal. B 277 (2020) 119232.
[47] Y. Cao, H. Li, J. Jin, Y. Li, T. Feng, W. Wang, B. Dong, L. Cao, An effective photocatalytic hydrogen evolution strategy based on tunable band gap $(CuIn)_xZn_{2(1-x)}S_2$ combined with amorphous molybdenum sulfide, New J. Chem. 45 (16) (2021) 7278–7284.
[48] B.W. Sun, J.K. Wu, W.J. Wang, H. Wang, Y.Y. Li, Z.Y. Guo, Y.L. Geng, H.F. Lin, L. Wang, Efficient visible-light-driven H_2 evolution induced by P-doped $Cd_{1-x}Zn_xS_2$ porous nano-spheres decorated with Ni_2P and reduced graphene oxide, Appl. Surf. Sci 542 (2020), 148542.
[49] D. Zhang, Y. Guo, Z. Zhao, Porous defect-modified graphitic carbon nitride via a facile one-step approach with significantly enhanced photocatalytic hydrogen evolution under visible light irradiation, Appl. Catal. B 226 (2018) 1–9.
[50] K. Ypatia, P. Athanasia, F. Zacharias, S. Maria, Ioannis, Solar photocatalytic degradation of bisphenol A with CuO_x/$BiVO_4$: Insights into the unexpectedly favorable effect of bicarbonates, Chem. Eng. J. 318 (2017) 39–49.
[51] C. Guo, G.E. Ming, L.U. Liu, G. Gao, Y. Feng, Y. Wang, Directed synthesis of mesoporous TiO_2 microspheres: catalysts and their photocatalysis for bisphenol A degradation, Environ. Sci. Technol. 44 (2010) 419–425.
[52] Y. Ding, Z. Ping, H. Tang, Visible-light photocatalytic degradation of bisphenol A on $NaBiO_3$ nanosheets in a wide pH range: A synergistic effect between photocatalytic oxidation and chemical oxidation, Chem. Eng. J. 291 (2016) 149–160.